C VI Lyman line profiles from 10-ps KrF-laser-produced plasmas

Y. Leng,* J. Goldhar, and H. R. Griem
Institute for Plasma Research, University of Maryland, College Park, Maryland 20742

Richard W. Lee
Lawrence Livermore National Laboratory, Livermore, California 94550

(Received 21 April 1995)

Plasmas with densities $\lesssim 10^{22}$ cm^{-3} and electron temperatures $T_e \lesssim 200$ eV were produced near solid graphite targets that were laser irradiated at approximately 10^{15} W/cm^2, with a $\sim 10^{11}$ W/cm^2 prepulse from amplified spontaneous emission. Photographic spectra taken nearly side-on within $\lesssim$ 0.1 mm from the target surface show strong H-like lines corresponding to $n = 2$, 3, and 4 to $n = 1$ transitions and weaker He-like lines with full width at half maximum widths $\lesssim 4$ eV. The Lyman-α line is optically thick. A five-layer model with high-electron-density and electron-temperature core layers and less dense and cooler outer layers was used for simulation. Central layers with high T_e contribute most of the emission while outside cooler layers cause an absorption dip in the central part of the Lyman-α line. Asymmetrical self-reversal is interpreted by radial expansion. A plasma-induced line shift was evident in some of the experimental line profiles, especially for the asymmetrical and strongly shifted Lyman-γ line of C VI ions. Time-dependent rate equations were solved for checking the assumed local-thermodynamic-equilibrium condition for plasmas with adiabatic expansion cooling.

PACS number(s): 52.25.Nr, 32.70.Jz, 52.70.La

I. INTRODUCTION

Plasma spectroscopy remains a very useful tool in the determination of densities in laser-produced plasmas, especially for supradense plasmas related to inertial confinement fusion and soft-x-ray laser research, where other diagnostics fail [1]. The usual method is to fit calculated line profiles to experimental results. Spectroscopic experiments are therefore needed to check and optimize current theoretical and computational models.

Further, line broadening prediction plays a significant role in calculating the gain coefficients of some soft-x-ray laser transitions, where correct modeling can define promising transitions [2–4]. In return, soft-x-ray lasers can be used to diagnose very dense plasmas [5–7], where visible and uv lasers fail due to their wavelengths being longer than the critical value for absorption λ_p, as determined by the plasma frequency [2].

Soft-x-ray laser research and potential applications were surveyed by Elton in 1990 [2]. Much progress has been made over the past 20 years in searching for new soft-x-ray transitions, excitation schemes, and theoretical models. Collisionally excited soft-x-ray lasing has been demonstrated by using very large laser pumping facilities [8]. Also, highly ionized recombining plasmas have the demonstrated potential for developing soft-x-ray lasers requiring a lower driving energy [9–11]. An alternative approach for achieving compact soft-x-ray lasers employs fast recombination following optical-field ionization of a relatively cold plasma [12–14].

Laser-produced dense plasma and soft-x-ray laser research has been greatly facilitated by the recent dramatic advances in picosecond and subpicosecond laser technology [15]. Picosecond and subpicosecond table-top lasers [16–18] generate pulses with shorter duration and higher peak power density than were available from the large lasers in the early 1980s. Focusing such intense short laser pulses onto a solid target produces plasmas with an electron density near solid density. For a subpicosecond laser pulse, the energy coupling is very inefficient due to the high reflectivity from the mirrorlike hot plasma surface. The peak reflectivity is approximately greater than 90%, even though recent work has shown that a higher coupling efficiency is achievable by using a grating structure or porous surface [19]. However, for a picosecond laser pulse of the type used here, the energy is coupled to the plasma during the plasma expansion phase. The gradient in electron density aids energy absorption, and a high-electron-temperature plasma can be produced. To couple the laser to higher-density plasmas, a short wavelength laser is required, due to the strong reflection from the critical density surface. About 50% absorption can be achieved for 12-ps uv pulses with a peak power density of 10^{15} W/cm^2 [20], although this may depend on prepulse and other details.

There have been several spectroscopic studies on laser-produced plasmas in this laboratory using longer, nanosecond, laser pulses [21–24]. Since the laser energy was coupled to the plasma after the expansion, only relatively low density (approximately 10^{20} cm^{-3}) plasmas

*Present address: Fusion Lighting Inc. 15700 Crabbs Branch Way, Rockville, MD 20855.

were formed due to the low peak power density and long laser wavelength (e.g., 694 nm) [21]. Also, the pulse duration of 20 ns was too long for studying the recombining plasma. Our present 10-ps KrF laser is optimally suited for spectroscopic study of the high-density recombining plasmas due to its higher peak power density of 10^{15} W/cm^2, high-energy coupling efficiency due to the short-pulse duration and short wavelength of 248.6 nm, in addition to its low construction and operation costs.

In this paper we report on an experimental study of C VI Lyman-line profiles from plasmas produced by 10-ps KrF laser pulses. Time-integrated soft-x-ray spectra, which were spatially and spectrally resolved, were obtained. To interpret the results, a five-layer, cylindrically symmetric model was used to simulate the line profiles and shifts in the inhomogeneous, transient plasma. The central high-electron-density and high-temperature layers contributed most of the broadened line emission, while the outer cooler layers caused a self-absorption dip in the Lyman-α line. A plasma shift was included to improve fitting of the experimental line profiles, especially for the asymmetrical and shifted Lyman-γ line. This model depends on near–local thermodynamic equilibrium (LTE) conditions, which was verified by solving coupled atomic physics rate equations numerically.

Section II briefly describes the experimental setup, which consists of three excimer lasers and a dye laser system, a soft-x-ray pinhole camera, a soft-x-ray grazing-incidence spectrograph, as well as collecting optics and detectors. Section III is divided into three subsections. Section III A presents the results of the space-resolved soft-x-ray spectroscopy. Section III B presents the investigation of the C VI Lyman-line profiles, which includes brief descriptions of the Stark-broadened line shape and plasma polarization shift calculations, a detailed description of the multilayer model, numerical simulations, and comparisons with observed line profiles. Section III C is dedicated to the study of the validity of LTE for multilayer modeling, which includes the time-dependent atomic physics rate equations, discussions of plasma cooling, and numerical simulations.

II. EXPERIMENT

A detailed description of this 10-ps KrF discharge laser system is given elsewhere [25]. The output from a XeCl excimer laser with an energy of 20 mJ and a duration of 20 ns was used to pump a 10-ps dye laser system. A simple quenched dye laser and a holographic distributed feedback dye laser were used to generate 10-ps pulses at 497.2 nm. After frequency doubling in a β-BaB_2O_4 crystal, the weak seed pulse was amplified by the first KrF amplifier to an energy of 20 mJ. A vacuum spatial filter was used to reject most of the amplified spontaneous emission (ASE) from this amplifier. The second KrF amplifier gave a final energy output of approximately 100 mJ with a duration less than 10 ps.

The ASE from the second KrF amplifier could generate low-temperature and low-ionization-stage (up to C^{2+} ions) plasmas with relatively low electron density. However, only a small portion of the total 1–2-ns ASE, preceding the 10-ps pulse, called the prepulse, affects the plasma generation. Nam *et al.* [26] made detailed studies of the effect of the prepulse on plasma generation and found that a reduction of the prepulse energy resulted in a higher-temperature plasma. From our measurements, the total energy of ASE was less than 25% of the energy in a 10-ps pulse for a fresh laser gas mixture and less than 5% for an old mixture. After considering the larger focal spot (approximately greater than 130 μm, instead of approximately less than 30 μm for the 10-ps pulse being discussed below) of ASE, the power density ratio of the 10-ps short pulse to ASE was greater than 10^4 and the effective prepulse consisted of less than 5% of the total energy of ASE, or about 1% of the main pulse energy.

The peak power density of a focused laser beam is an important parameter for generating highly ionized plasmas. It determines the contributions from direct optical-field and electron-collisional ionizations. Three quantities are needed in calculating this peak power density, the pulse energy, the pulse duration, and the spot size of the focused laser beam. The energy of a short laser pulse is easily measured by an energy meter and the pulse duration by a commercial streak camera. The spot size could not be determined by simply imaging the visible emissions from the focused laser beam because this size was much larger than the actual spot size of the soft-x-ray emission. Hence a soft-x-ray, 25-μm-diam pinhole camera was built and used for the measurement of the spot size of the focused laser beam.

For emissions at a short wavelength of approximately 40 Å, the diffraction effect of the 25-μm-diam pinhole is still very significant. Such a pinhole allows a few Fresnel half-wave fronts to pass through. Hence we used Fresnel diffraction theory to calculate the pinhole diffraction profile of the soft-x-ray emissions. Comparing with the numerical results, we concluded that the spot size of the focused laser beam is less than 30 μm with a lens of 30 cm focal length, which is consistent with the optical measurement of the beam divergence of less than 4×10^{-5} rad, but provides only an upper limit.

For spectroscopic diagnostics of the 10-ps KrF laser-produced plasmas, we employed a McPherson Model 247, 2.217-m high spectral resolution grazing-incidence soft-x-ray spectrograph, with a gold-coated grazing-incidence focusing mirror located approximately 30 cm from its entrance slit, as shown in Fig. 1. This collecting mirror with a demagnification close to 1.5:1 increased the spectrograph's collection solid angle without sacrificing its spatial resolution. With an entrance slit size of 10 μm, this setup had a spatial resolution at the plasma of better than 30 μm. For a 2400 lines/mm gold-coated grating, a spectral resolution of better than 50 mÅ was achieved. A solid graphite cylindrical target of 1 in. diameter, positioned by two collars separated by two inches for a precision of 12 μm, was driven by a stepper motor. A fresh surface was provided for each laser shot. The laser beam was focused by a 30-cm-focal-length fused-silica lens to a peak power of approximately 10^{15} W/cm^2.

Although the optimized grazing-incidence angle for re-

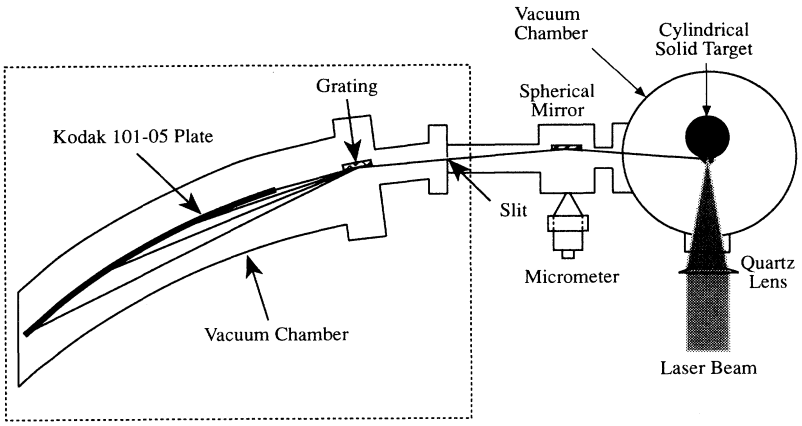

FIG. 1. Experimental setup for soft-x-ray spectroscopy with a 2.2-m grazing-incidence spectrograph.

flection efficiency was 88°, we found that it was very difficult to align this spectrograph to view the tiny plasma produced by our 10-ps KrF laser pulse. We therefore reconfigured the spectrograph to a grazing-incidence angle of 86° allowing us to install an exit slit and to monitor the soft-x-ray emission of zeroth-order diffraction. For alignment with the target, we first used a He-Ne laser to backlight the grating, the focused laser light passing through the entrance slit of the spectrograph. The emergent light then was refocused onto the target surface by the grazing-incidence collecting mirror. The system was then aligned approximately, but still far from the exact position of the plasma compared to the plasma size, due to the diffraction limit of visible light. Next we mounted a photomultiplier on the scanning exit slit, along with 2000 Å of aluminum filtering to reject low photon energy radiation. We then optimized the alignment by maximizing the signal from the soft-x-ray radiation at the zeroth order of the spectrograph.

The 2.2-m grazing-incidence spectrograph was placed on a table with its two front legs on a translation stage. The position of the spectrograph was indicated by a micrometer with respect to the target chamber. The micrometer had a precision of better than 10 μm. Spatially resolved spectra were obtained by moving the spectrograph to look at different parts of the plasma. The time-integrated spectra were recorded on Kodak 101-05 photographic plates. The relative intensity calibration showed that our spectra fell in the linear range [27].

III. RESULTS AND DISCUSSION

A. Space-resolved soft-x-ray spectroscopy

As described in the preceding section, a McPherson 2.2-m grazing-incidence spectrograph was used for improved spectral and spatial resolution. A mask with an adjustable slot width of 2 mm was installed perpendicularly to the entrance slit and advanced to different positions to obtain multiple spectra on a single Kodak 101-05 photographic plate. With an entrance slit width of 10 μm, this spectrograph has a spectral resolution of better than 50 mÅ in the wavelength region of interest.

We began the spatially resolved experiments with the spectrograph viewing the target surface. The 10-ps KrF laser was fired with a repetition rate of 0.2 Hz. The spectra corresponding to each spatial location were time integrated over an accumulation of 1500 shots with an energy of approximately 100 mJ per shot. The soft-x-ray spectra, with high spectral and spatial resolutions, from the plasmas on the target surface (a) and at different distances (b)–(d) from the target are shown in Fig. 2.

In Fig. 2(a), the Lyman-α ($1s$-$2p$) line of hydrogenlike carbon exhibits opacity broadening and asymmetrical reversal caused by self-absorption in the radially expanding plasma. The Lyman-β ($1s$-$3p$) and Lyman-γ ($1s$-$4p$) lines show significant broadening caused by the Stark effect. Figure 2(b) shows the spectrum of a similar plasma about 40 μm from the target surface. The Lyman lines are significantly narrower than those in Fig. 2(a). The expansion of the plasma results in a rapid decrease in the electron density and temperature at some distance from the target surface. The observed changes from (a) to (b) suggest that the initial spot size of the plasma produced by our 10-ps KrF laser pulse was much less than 40 μm because the linewidths and intensities of the Lyman lines drop significantly and heliumlike carbon lines become evident. Figure 2(c) shows the plasma spectrum 80 μm from the target surface and Fig. 2(d) shows the spectrum of similar plasmas 120 μm from the target surface. Any line broadening caused by the Stark effect is below the instrumental resolution at the larger separations. Therefore, we will limit our discussion to the hydrogenlike carbon Lyman lines from plasmas near the target surface, as those in Fig. 2(a).

B. C VI Lyman-line profiles

1. Stark-broadening calculations

For a nonhomogeneous plasma, both the Inglis-Teller limit [28] and the measurement of linewidths caused by

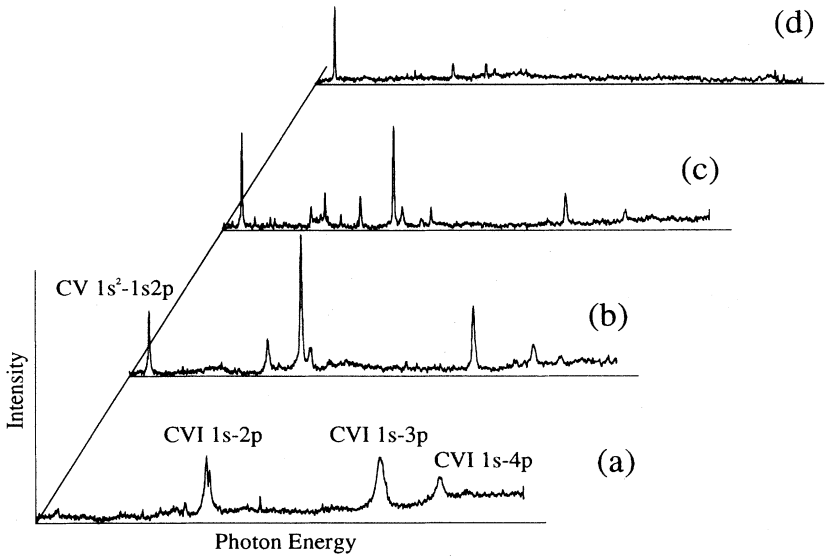

FIG. 2. Space-resolved time-integrated soft-x-ray spectra of highly ionized carbon plasmas (a) on the target, (b) 40 μm from the target, (c) 80 μm from the target, and (d) 120 μm from the target.

Stark effect give only qualitative, averaged values for the electron density. In addition, most of the previous Stark-profile calculations did not include the dynamical correction to broadening by ions and the tabulated fractional widths of Stark profiles are too sparse for the quantitative evaluation of the plasma conditions, such as the electron densities, and their spatial extension. Some recent studies suggest [29], for a highly ionized plasma with high electron temperature and density, that dynamical corrections are needed to perform reliable comparisons with experiments, especially for Lyman-α lines.

The computation of the spectral shape of ionic lines emitted from plasmas requires a complicated combination of the electron collision operator matrix elements for the various Stark components, the Stark effect due to the ion microfield at the radiator, and the fluctuations of this microfield. The calculational method [29–32] used to obtain the shape of the lines was based on the usual separation of the effects on the radiating ion of (a) the fast electron collisions or impacts and (b) the quasistatic electric fields from slowly moving ions. This second approximation considers the perturbing ion microfield at the radiating ion, which splits the line into a number of Stark components, or "radiative channels," undergoing spontaneous emission. Electron collisions result in the homogeneous broadening of each Stark component of the radiative transition and some interference between the components [29]. If the ion microfield does not change during the time of interest for the radiation process, the perturbing ions can be considered to be static during the radiation process and an average over the microfield perturbations at the radiator is performed to obtain the inhomogeneous broadening contribution to the line shape. Otherwise, if the ion microfield is fluctuating, the radiation would be transferred from channel to channel within each line during this transition period and the profile would become a complex mixture of the radiative components of the static calculation. The ion dynamics was simulated in the code by the dynamical mixing of radiative components obtained from the static calculation for each line transition separately. The idea behind this model is the assumption that the component mixing is the result of sudden microfield fluctuations at the radiator.

2. *Plasma polarization shift*

Nguyen *et al.* [33] have developed a model of a confined ion in a self-consistent field and performed a quantum-mechanical impact calculation to obtain electron-produced linewidths and shifts. In their calculation, the monopole, dipole, quadrupole, and octopole interactions have been taken into account. The numerical analysis shows that the monopole interaction plays a leading part in the redshift of the Lyman lines. The higher orders of the multipolar expansion occur only in the higher members of the spectral series ($n \geq 3$), slightly reducing the monopole interaction redshifts. The spectral line shift in eV can be given in the form

$$\hbar\Delta\omega(nl \rightarrow 1s) = \left[-\frac{10^{-22}[N_e\,(\mathrm{cm}^{-3})]}{Z_E^2} D(n,l,T)\ [\mathrm{eV}] \right], \tag{1}$$

where the minus sign means a decrease in emitted photon energy, or a redshift. The factor $D(n,l,T)$ is tabulated [33]. For example, the Lyman-γ line emission from a plasma with an electron density of 10^{22} cm^{-3} and an electron temperature of 200 eV would have a plasma shift of -1.78 eV. This is mostly due to the excess negative charge in the vicinity of highly charged emitting ions, hence the name polarization shift [30].

Goldsmith *et al.* [34] studied the plasma shifts of C VI, N VII, and O VIII resonance lines with the Omega laser system at the University of Rochester Laboratory for Laser Energetics and obtained upper limits for the

shifts. The plasmas produced by our laser pulses, with higher electron density, a small spatial extension, and relatively low charge Z_E, are prime candidates for comparison with theoretical calculations [33]. The Lyman-β and -γ lines have smaller absorption oscillator strengths, larger widths (compared with the Lyman-α line), and much larger shifts. This makes the comparison of measured and predicted shifts much easier, and one can neglect their opacity broadening. We also note that the quadrupole corrections to the quasistatic broadening by ions are small compared with the electron-produced shifts [35] and that any dielectronic satellites may be estimated to have relative intensities of less than or about 0.1% of the parent lines [36].

3. *Multilayer model*

Line broadening due to Stark effect is very sensitive to the electron density. In order to analyze the soft-x-ray spectra emitted from an inhomogeneous plasma, a model accounting for the spatial distribution of the electron density is needed [37]. A five-layer, cylindrically symmetrical model was introduced for the plasmas produced by our laser pulses. In this model, electron densities were constrained to 10^{22} cm^{-3} for the central layer and 3×10^{21}, 10^{21}, 3×10^{20}, and 10^{20} cm^{-3}, respectively, for the other four layers. The model permitted that the effective electron temperatures and radii of the shells are independently determined consistent with the constraint. We employ the assumption of LTE for the model and show in Sec. III C that for the critical central regions, LTE is valid. The sizes of the two central layers with high electron densities were determined from soft-x-ray pinhole camera measurements, using an approximately 25-μm-diam aperture. A schematic of the multilayer model is shown in Fig. 3.

Because of the strong astigmatism of the grazing-incidence spectrograph, the spectral lines on the Rowland circle correspond to the loci of the horizontal foci. There is no spatial resolution vertically (along the direction of the entrance slit) for a grazing-incidence spectrograph. Instead of using cylindrical symmetry, we therefore converted the model into a nine-layer, one-dimensional (1D) planar problem, as shown in Fig. 3. The thicknesses of these 1D layers correspond to the differences of the radii of the neighboring shells and the volume of each layer or the total number of electrons in each layer is calculated from that of the corresponding cylindrical shell. The choice of parameters will be discussed below.

In order to find the final line shapes of the soft-x-ray emissions from this nine-layer model plasma, we first calculate the intensity $\triangle I$ of the electromagnetic radiation from each sublayer of thickness $\triangle x$, without considering self-absorption from the sublayer itself, i.e., [38]

$$\triangle I(\omega, \Theta, x) = \frac{\hbar\omega^3 r_0}{2\pi c} \frac{g_n}{g_m} f_{mn} N_m(x) L(\omega, x) \triangle x, \quad (2)$$

where g_n/g_m is the ratio of statistical weights of lower and upper states of the line, respectively, $N_m(x)\triangle x$ is

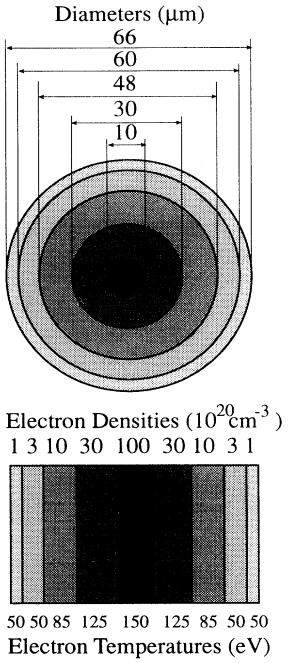

FIG. 3. Geometry of the multilayer model. In computer simulations, the outer layers in the planar model are actually enlarged to have the same volume as the corresponding cylindrical shells.

the total number of ions in the upper energy level per unit area and at a specific position x for this sublayer, and $\triangle x = 1$ μm here. We also need to calculate the total optical depth for each sublayer since absorption can strongly affect the emitted line profile,

$$\triangle\tau(\omega, x) = k'(\omega, x)\triangle x, \quad (3)$$

where $k'(\omega, x)$ is the effective line absorption coefficient given by [38]

$$k'(\omega, x) = 2\pi^2 r_0 c f_{mn} N_n(x) \times \left\{1 - \exp\left[-\frac{\hbar\omega}{kT(x)}\right]\right\} L(\omega, x). \quad (4)$$

Here r_0 is the classical electron radius, f_{mn} is the absorption oscillator strength, $N_n(x)$ is the ground-state population density for the Lyman series, and $L(\omega, x)$ is the calculated Stark-Doppler line profile. The $\{1-\exp[-\frac{\hbar\omega}{kT(x)}]\}$ factor corrects for induced emission, which is found to be unimportant for our conditions.

The optical depth measured from a point b near the observer toward the center of the plasma is just the sum of all the corresponding 1-μm sublayers

$$\tau(\omega, x) = \sum_x^b k'(\omega, x)\triangle x. \quad (5)$$

Since there is no intensity entering the opposite boundary ($x = a$) of the plasma, i.e., $I(\omega, \Theta, a) = 0$, the final power of the emission $P(\omega, \Theta, b) = 0$ from this nonhomogeneous multilayer plasma is

$$P(\omega,\Theta,b)=\sum_{a}^{b}\triangle I(\omega,\Theta,x)A(x)\exp[-\tau(\omega,x)]. \quad (6)$$

Here $A(x)$ is the area of the sublayer converted from the cylindrical symmetry and $A(x)\triangle I(\omega,\Theta,x)$ is the total power of the soft-x-ray emission from this one sublayer at a specific position x, without introducing the self-absorption from this sublayer itself. However, $P(\omega,\Theta,b)$ is not the final profile we would observe because the spectrograph has a finite spectral resolution. In order to make a comparison with the experimental result, we convolved the final theoretical profile with the instrumental function, assumed to have a Gaussian profile.

The computation of the spectral line shapes that we discussed in Sec. III B 1 did not include the plasma polarization shift. Table I lists the calculated plasma energy shifts (in eV) for the five electron densities at the electron temperature of 150 eV by referring to the table of the line-shift factor $D(n,l,T)$ in Ref. [33]. For a plasma with a lower electron temperature we expect larger plasma shifts. These shifts were introduced to the calculated line profile by shifting the entire profile in a given sublayer to the low-photon-energy direction.

A blueshifted narrow absorption dip in the Lyman-α line was observed to be much narrower than the full width at half maximum (FWHM) of the line. It therefore corresponds to the lower electron density and temperature outer plasmas with abundant ground-state population densities. The radially expanding plasma cools and becomes less dense as it moves from the region of the focal spot; this indicates that the outer layer absorption will be blueshifted. We introduced the expanding plasma shift effect by shifting the calculated Stark profiles of outer cooler layers, which were moving towards the spectrograph, in the direction of higher photon energy (blueshift), and outer cooler layers, which were moving away from the spectrograph, in the direction of lower photon energy (redshift). We estimated the relative velocity of the expanding plasma to be approximately greater than 1×10^{7} cm/s from the spectral profile of the Lyman-α line and then converted to photon energy shifts (approximately 0.1 eV) in our numerical simulation.

4. Numerical simulations and comparison with observed line profiles

The LTE conditions assumed for the individual plasma layers in this section will be validated in Sec. III C. The simulation starts with the calculation of the partition functions. From the given electron density and temperature we calculated the Debye radius ρ_D, the reduction of the ionization energy $\triangle E_{\infty}^{z-1}$, and the principal quantum number $n_{\max}$ of the last level contributing to the partition function. The Boltzmann factors, Saha equations, and electric charge neutrality were used to calculate the ion population densities in the different ionization stages.

Optical depth, which depends only on the population densities and the thickness of the layer, was calculated for each 1-μm segment of the nine individual layers. Following the discussion in Sec. III B 3, we calculate optical depths measured into the plasma from the observation point for all photon energies of interest, as in Eq. (5).

For obtaining the intensities of the lines from this multilayer plasma, we first calculated the emission for each 1-μm depth and unit area layer segment for the nine individual layers without introducing the self-absorption, as in Eq. (2). This intensity depends on the total number of ions in the upper energy level, which is equal to the population density times the volume segment. The conversion from the cylindrical symmetry to one-dimensional symmetry resulted in a changing value of the area, depending on its location. Following the discussion in Sec. III B 3, we finally calculated the theoretical line profile as in Eq. (6).

In order to make a comparison with the experimental results, we convolve the theoretical line profile with the instrumental function. The computed spectral resolution of the spectrograph in photon energy (eV) units was then taken to be the FWHM of the Gaussian profile, which was normalized to maintain a unit area under the line profile. The convolution of the theoretical line profile and the computer-generated Gaussian profile resulted in the final line profile of the emission from the plasma, which was used to make comparisons with the experimental results.

The results of our multilayer model simulation are shown in Figs. 4(a)–4(c). Both the receding Doppler shift and the plasma polarization shift are included in these figures. The numerical programs for the three Lyman lines used the same nine-layer parameters for all lines, as shown in Fig. 3. In the numerical simulation, the Lyman-α line is very sensitive to the electron temperature of the individual layers and the Lyman-β line is very sensitive to the electron density of the layers. The electron temperatures could not be the same; otherwise there is no dip in the Lyman-α line. The electron densities could not all be 10^{22} cm^{-3} because this would give a larger FWHM than the actual value.

Understanding the blueshifted absorption dip in the Lyman-α line required that the outer layers with lower effective electron densities have low electron temperatures to provide sufficient ground-state population densities for adequate self-absorption. Understanding the missing central dip in the observed profile of the Lyman-β line required that the outer layers with low electron densities should have still sufficiently high temperatures to provide the excited-state population densities for filling out the central dip in the calculated line profiles. Finally, the broadening of the Lyman-γ line caused by the differences in the plasma polarization shifts between various layers also required that the plasma should have adequate upper level population densities across the layers. Extensive

TABLE I. Calculated plasma polarization shifts (in eV) for the C VI Lyman lines at kT = 150 eV.

Lyman series	Electron density (cm^{-3})				
	10^{20}	3×10^{20}	10^{21}	3×10^{21}	10^{22}
L_α	0.001	0.004	0.013	0.04	0.13
L_β	0.006	0.019	0.06	0.19	0.60
L_γ	0.018	0.055	0.18	0.55	1.80

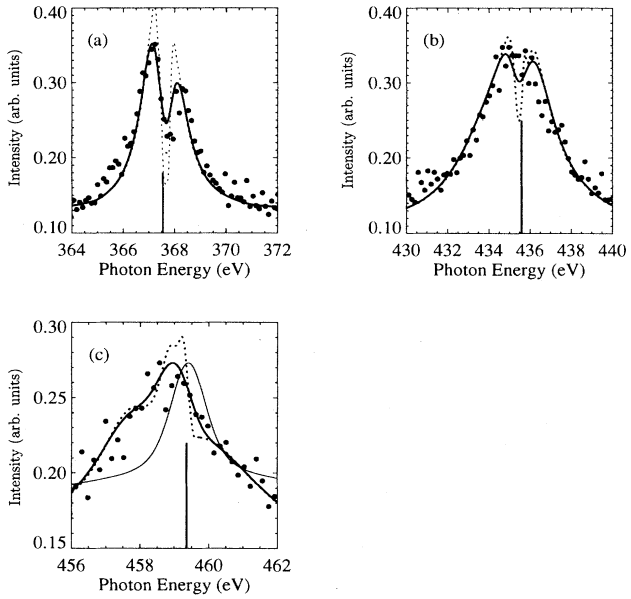

FIG. 4. C VI (a) Lyman-α, (b) Lyman-β, and (c) Lyman-γ line profiles. Dots are the experimental data points, the dashed line is the theoretical line profile, and the solid line is the final line profile after convolution with the instrumental function. The thin-solid line in (c) represents the final Lyman-γ profile not including the plasma shifts.

tests were carried out before a solution was reached and a combination of the electron temperatures and densities was finally chosen that satisfies all the constraints.

To clarify the additional effect of the shifts, we show in Fig. 4(c) a final calculated profile not including the plasma shifts. A consistent solution was made to fit all three lines and our multilayer model gave the agreement shown, when allowing for plasma shifts. Considering also the limited resolution of the spectrograph and the Doppler line broadening, without the shifts the Lyman-γ line would be narrower by a factor of 2.

C. Validity of LTE for multilayer modeling

In our multilayer model we assumed that the plasmas were in LTE. Due to the high electron density in the central two layers this assumption may be valid in steady state. However, for outside layers with lower electron densities, the LTE conditions are satisfied only for levels with larger principal quantum numbers than those studied. Since the plasmas were transient, having a time scale of approximately 1 ps, the populations may not reach their steady-state values in this time. In order to ascertain the appropriateness of steady-state populations in the excited and ground levels for these transient plasmas we could use either calculated collisional-radiative ionization and recombination coefficients [39–41] or solve the coupled atomic physics rate equations. Since the collisional-radiative coefficients listed in tables [41] are too sparse and it is almost impossible to interpolate values with better than order of magnitude accuracy, we employ rate equation solutions.

The temporal evolution of the population density of a level with principal quantum number p is described by the rate equation [42]

$$\frac{d}{dt}n(p) = \sum_{q<p} C(q,p)n_e n(q) - \left[\left\{\sum_{q<p} F(p,q) + \sum_{q>p} C(p,q) + S(p)\right\}n_e + \sum_{q<p} A(p,q)\right]n(p) + \sum_{q>p}\{F(p,q)n_e + A(q,p)\}n(q) + \{\alpha(p)n_e + \beta(p)\}n_z n_e, \quad (7)$$

where $C(p,q)$ and $F(q,p)$ are the excitation rate coefficient by electron collisions from level p to q and its inverse deexcitation rate coefficient, respectively, $A(p,q)$ is the spontaneous transition probability from p to q, $S(p)$ and $\alpha(p)$ are the ionization rate coefficient and the three-body recombination rate coefficient for level p, respectively, $\beta(p)$ is the radiative recombination rate coefficient, n_z is the particle density of the fully stripped ion, and n_e is the electron density. The quasi-steady-state solution of Eq. (7) is derived by setting the left-hand side to zero and solving the coupled linear equations consistent with quasineutrality at the assumed electron density.

For the instantaneous population densities of the excited and ground levels of the plasma, we have to solve coupled ordinary differential equations, such as Eq. (7), using approximate expressions for the rate coefficients [42,43]. However, we still need initial values for the population densities.

There are two major processes contributing to the ionization of atoms and ions, namely, optical-field ionization and electron-collisional ionization. For our discussion, we need to find out how long it would take to fully ionize the carbon atoms. First, we consider the optical-field ionization process due to the high field from the focused laser beam. The optical field strength E is related to the laser intensity I by

$$E = \sqrt{\frac{2I}{\varepsilon_0 c}} = [27.4\sqrt{I}\ (\mathrm{V/cm})], \quad (8)$$

where I is the laser intensity in W/cm^2, ε_0 is the electric permitivity, and c is the speed of light. The peak power density on the focal spot of our 10-ps KrF laser pulse is approximately 10^{15} W/cm^2, corresponding to electric fields of 8.7×10^8 V/cm, approaching the atomic field strength of 5.1×10^9 V/cm in the ground state of hydrogen. These very strong fields from the focused laser beam imply that this optical-field ionization process is

very important for the initial ionization of atoms.

The ionization processes for strong fields can be treated as follows. As the laser intensity rises to its maximum value and ionization proceeds stepwise, the remaining bound electrons located in the center of the focal spot have high natural frequencies compared with that of the driving laser. Therefore, the high-field ionization rates depend very weakly on frequency and can be computed by using dc tunneling rates. The level of ionization reached during the laser pulse can be estimated using a simple Coulomb-barrier model. This Coulomb-barrier model leads to a threshold intensity [44]

$$I_{\rm th} = \left[\frac{2.2 \times 10^{15}}{Z^2} \left\{ \frac{U_i}{27.21} \right\}^4 ({\rm W/cm^2}) \right], \qquad (9)$$

where Z is the charge state after the optical-field ionization and U_i is the ionization potential of the charge state $Z-1$. $I_{\rm th}$ was obtained by requiring an ionization rate of 10^{12} s^{-1}. Using the peak power density of our laser beam, we find that charge states 2 ($U_1 = 24.4$ eV) or even 3 ($U_2 = 47.9$ eV) can be reached through high-field ionization in a few picoseconds.

For a solid graphite target, the number density of carbon atoms is approximately 10^{23} cm^{-3}. After each atom gives up one electron through the optical-field ionization, the electron density of the initial plasma could reach approximately 10^{23} cm^{-3}, more than the critical density of 1.6×10^{22} cm^{-3}. The contribution from electron collisional ionization then becomes very important. Our numerical simulation of Eq. (7) suggests that the ionization processes reaches a steady state before the end of the laser pulse, i.e., approximately less than 10 ps, corresponding to fully stripped carbon ions [45].

After the laser pulse turns off, the plasma enters its recombination phase. The three important cooling mechanisms are plasma expansion, thermal conduction, and radiation. We neglect the thermal conduction cooling based on the work by Milchberg *et al.* [46] at even higher electron density. The radiative cooling also can be neglected [45]. We treated expansion cooling as an adiabatic expansion. For a plasma with a velocity of 2×10^7 cm/s [45], the lifetime of this plasma is approximately 30 ps, i.e., longer than the laser pulse duration.

Dynamical evolutions of the electron density, bare ion density and the excited and ground levels of the H-like ions were therefore also calculated for a recombining plasma [47]. The initial electron density was approximately 10^{22} cm^{-3}, the temperature approximately 150 eV, and we assumed that all the ions were bare carbon nuclei. It took approximately less than 1 ps for the excited states of C VI to reach steady state and approximately less than 4 ps for the ground state to reach steady state. Importantly, the excited-state steady-state population densities are within 2% of the LTE population densities. The ground-state is overpopulated compared with the LTE value by about 34%, partly because we did not include self-absorption processes in the atomic rate equations. The inclusion of self-absorption would have the effect of reducing the radiative decay rate, thus maintaining more ions in the excited states and more ions as bare nuclei. Therefore the LTE conditions are good assumptions for the central layers with high electron densities. For the outer layers deviations from LTE populations are much larger and their temperatures will be only effective values that will provide ground-state populations similar to actual densities, as necessary for the correct simulation of the spectrum.

The plasma produced by our 10-ps KrF laser pulse is transient. After the laser pulse ceases, the plasma enters the recombining phase while it is expanding. As already discussed, the most important cooling mechnism is adiabatic expansion. We introduced the temporal variation of the electron temperature, as shown in Fig. 5, by assuming an ideal gas for electrons expanding with a mean velocity of 2×10^7 cm/s. The variation of the electron density was taken into account after each step of expansion, as well as that of the bare ion density. The total number of H-like ions was derived from the neutrality condition. The excited-state population densities were calculated to decrease by about one order of magnitude in 60 ps. The Lyman-line radiation effectively ends earlier, with an estimated $1/e$ decay time of about 40 ps.

IV. SUMMARY AND CONCLUSIONS

For spectroscopic diagnostics of the 10-ps KrF laser-produced plasmas, we employed a 2.2-m grazing-incidence spectrograph that has a spectral resolution of approximately less than 50 mÅ and a spatial resolution of approximately less than 30 μm. The highly spectrally and spatially resolved soft-x-ray spectra indicated that there were mostly H-like carbon emissions near the target surface, with significantly broadened Lyman lines. As the plasma expanded, these lines became narrower and weaker and the He-like carbon emissions became more prominent. This suggested that the plasma began with mostly bare and H-like ions. As the plasma expanded, the recombination takes place into the highly lying states

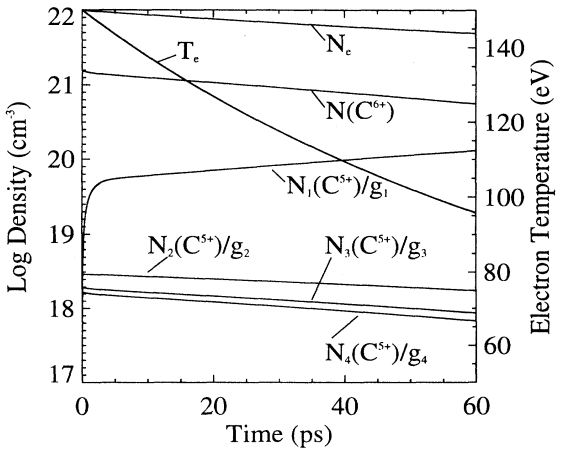

FIG. 5. Time-dependent population densities of a recombining plasma with adiabatic expansion and initial $T_e = 150$ eV and $N_e \approx 10^{22}$ cm^{-3}. Log denotes $\log_{10}$.

followed by cascading into lower bound states. The opacity broadening and blueshifted absorption dip of the H-like carbon Lyman-α line indicated that even for a 10-ps laser-produced plasma with a very small spatial extent, self-absorption (optical thickness) must be considered.

A five-layer, cylindrically symmetric model was introduced for simulating the line profiles and shifts in the inhomogeneous-transient plasmas. In our model, the electron densities were chosen to be 10^{22} cm^{-3} for the central core and 3×10^{21}, 10^{21}, 3×10^{20}, and 10^{20} cm^{-3}, respectively, for each of four outer layers. The electron temperatures used for numerical simulation are 150 eV for the central core and 125, 85, 50, and 50 eV, respectively, for the four outer layers. LTE conditions were assumed to hold for these five layers independently, which are not rigorously valid for the outer layers with lower electron densities, but provide the essential ground-state population important for these outer layers. The electron temperatures and densities and the radii of the shells are independently changeable. Calculated Stark-broadened line profiles with the dynamical correction of broadening by ions were used in our numerical simulation. The two central high-electron-density and temperature layers contributed most to the broadened line emission. The other three lower-electron-density and temperature layers produced the self-absorption dip with a narrow linewidth observed in the C VI Lyman-α line profile. The radius of the layer with an electron density of 3×10^{21} cm^{-3} was chosen to be 30 μm and the radius of the central layer was determined from a similar fitting of the C VI Lyman-β line profile, which is very sensitive to the electron density.

The opacity broadening of the C VI Lyman-α line was found to be very sensitive to the electron temperatures of the two central layers. The maximum optical depth at the peak of the C VI Lyman-α line was approximately greater than 24 in our numerical simulation. Inclusion of the plasma polarization shift, caused by screening by plasma electrons of the net nuclear (or "core") charge acting on the radiating electron, was required to improve the line profile fittings to the experimental data points, especially for the C VI Lyman-γ line. Omission of this effect and use of this line for density diagnostics under similar conditions could lead to overestimates of density by a factor of approximately 2. However, the corresponding bound energy level shifts are only approximately 1% of kT, i.e., not important for the thermodynamic plasma properties.

Time-dependent atomic rate equations were solved numerically to check the validity of LTE in our multilayer model. Optical-field ionization was found to be a very important process in the initial ionization stages for our power density of 10^{15} W/cm^2, by which doubly or even triply ionized stages can be reached in a few picoseconds. At one-half the critical density and $T_e = 200$ eV, it takes less than 2 ps to collisionally ionize H-like carbons to bare ions, which is consistent with our assumption that the recombining plasma consisted initially of all bare ions and electrons. Numerical simulations for the recombining plasmas showed that LTE was an appropriate assumption for the central layers with high electron densities in the muiltilayer model, which contribute most to the line emission. We determined that the most important cooling mechanism is adiabatic-expansion cooling, which gives a $1/e$ decay time of 40 ps to the Lyman-α line intensity. This time dependence was derived by using the temporal variations of the electron temperature and density in the atomic rate equation solution. This is longer than a recently measured decay time of approximately 15 ps for the Lyman-β line [48] from a 0.7-ps, (4×10^{16})-W/cm^2 KrF laser-produced plasma with negligible prepulse, but quite consistent with the longer decay time observed [48] in case a low-intensity, longer-pulse laser is used to generate a preplasma. Finally, although the optical field strength according to Eq. (8) is similar to the plasma microfield [30], no effects of these oscillating fields on the C VI Lyman line were observed, presumably because most of their emission occurs after the laser pulse.

ACKNOWLEDGMENTS

The authors would like to thank V. Yun and K. Diller for their expert technical assistance. We would also like to thank Ray Elton, Ben Welch, Juan Moreno, Howard Milchberg, Enrique Iglesias, and Samuel Goldsmith for useful suggestions and discussions. This research was jointly supported by the National Science Foundation and the Naval Research Laboratory.

[1] Hans R. Griem, Phys. Fluids B **4**, 2346 (1992).
[2] Raymond C. Elton, *X-Ray Lasers* (Academic, San Diego, 1990).
[3] Hans R. Griem, Phys. Rev. A **33**, 3580 (1986).
[4] J. C. Moreno, Hans R. Griem, S. Goldsmith, and J. Knauer, Phys. Rev. A **39**, 6033 (1989).
[5] L. B. DaSilva, J. E. Trebes, and R. Balhorn, Proc. SPIE **2102**, 158 (1993).
[6] L. B. DaSilva, J. E. Trebes, and R. Balhorn, Science **258**, 269 (1992).
[7] D. Ress, L. B. DaSilva, R. A. London, J. E. Trebes, S. Mrowka, R. J. Procassini, T. W. Barbee, Jr., and D. E. Lehr, Science **265**, 514 (1994).
[8] D. L. Matthews, P. L. Hagelstein, M. D. Rosen, M. J. Eckart, N. M. Ceglio, A. Hazi, H. Medicki, B. J. MacGowan, J. E. Trebes, B. L. Whitten, E. M. Campbell, C. W. Hatcher, A. M. Hawryluk, R. L. Kauffman, L. D. Pleasance, G. Rambach, J. H. Scofield, G. Stone, and T. Weaver, Phys. Rev. Lett. **54**, 110 (1985).
[9] S. Suckewer, C. H. Skinner, H. Milchberg, C. Keane, and D. Voorhees, Phys. Rev. Lett. **55**, 1753 (1985).
[10] C. O. Park, L. Polonsky, and S. Suckewer, Appl. Phys.

B **58**, 19 (1994).
[11] J. Zhang and M. H. Key, Appl. Phys. B **58**, 13 (1994).
[12] N. H. Burnett and G. D. Enright, IEEE J. Quantum Electron. **QE-26**, 2589 (1991).
[13] P. Amendt, D. C. Eder, and S. C. Wilks, Phys. Rev. Lett. **66**, 2589 (1991).
[14] G. L. Strobel, D. C. Eder, and P. Amendt, Appl. Phys. B **58**, 45 (1994).
[15] M. M. Murnane, H. C. Kapteyn, S. P. Kapteyn, and R. W. Falcone, Appl. Phys. B **58**, 261 (1994).
[16] W. Tighe, C. H. Nam, J. Robinson, and S. Suckewer, Rev. Sci. Instrum. **59**, 2235 (1988).
[17] T. S. Luk, A. McPherson, G. Gibson, K. Boyer, and C. K. Rhodes, Opt. Lett. **14**, 1113 (1989).
[18] B. Bouma, T. S. Luk, K. Boyer, and C. K. Rhodes, J. Opt. Soc. Am. B **10**, 1180 (1993).
[19] M. M. Murnane, H. C. Kapteyn, S. P. Gordon, J. Bokor, E. N. Glytsis, and R. W. Falcone, Appl. Phys. Lett. **62**, 1068 (1993).
[20] D. Riley, L. A. Gizzi, A. J. Mackinnon, S. M. Viana, and O. Willi, Phys. Rev. E **48**, 4855 (1993); see also R. Sauerbrey, J. Fure, S. P. Le Blanc, B. van Wonterghem, U. Teubner, and F. P. Schäfer, Phys. Plasmas **1**, 1635 (1994); Y. Al-Hadithi, G. J. Tallents, J. Zhang, M. H. Key, P. A. Norreys, and R. Kodama, *ibid.* **1**, 1279 (1991).
[21] E. J. Iglesias and H. R. Griem, Phys. Rev. A **38**, 301 (1988).
[22] E. J. Iglesias and H. R. Griem, Phys. Rev. A **38**, 308 (1988).
[23] J. S. Wang, H. R. Griem, and E. J. Iglesias, Phys. Rev. A **40**, 4115 (1989).
[24] Y. W. Huang, J. S. Wang, J. C. Moreno, and H. R. Griem, Phys. Rev. Lett. **65**, 1757 (1990).
[25] Y. Leng, V. E. Yun, J. Goldhar, and H. R. Griem, Rev. Sci. Instrum. **66**, 4045 (1995).
[26] C. H. Nam, W. Tighe, E. Valeo, and S. Suckewer, Appl. Phys. B **50**, 275 (1990).
[27] B. L. Henke, S. L. Kwok, J. Y. Uejio, H. T. Yamada, and G. C. Young, J. Opt. Soc. Am. B **1**, 818 (1984); B. L. Henke, F. G. Fujiwara, M. A. Tester, C. H. Dittmore, and M. A. Palmer, *ibid.* **1**, 828 (1984).
[28] D. R. Inglis and E. Teller, Astrophys. J. **90**, 439 (1939).
[29] A. Calisti, F. Khelfaoui, R. Stamm, B. Talin, and R. W. Lee, Phys. Rev. A **42**, 5433 (1990).
[30] Hans R. Griem, *Spectral Line Broadening by Plasmas* (Academic, New York, 1974).
[31] L. Godbert, A. Calisti, R. Stamm, B. Talin, R. W. Lee, and L. Klein, Phys. Rev. E **49**, 5644 (1994).
[32] A. Calisti, L. Godbert, R. Stamm, and B. Talin, J. Quant. Spectrosc. Radiat. Transfer **51**, 59 (1994).
[33] H. Nguyen, M. Koenig, D. Benredjem, M. Caby, and G. Coulaud, Phys. Rev. A **33**, 1279 (1986); see H. R. Griem, M. Blaha, and P. C. Kepple, *ibid.* **45**, 5600 (1990) for similar calculations for heliumlike argon.
[34] S. Goldsmith, H. R. Griem, and L. Cohen, Phys. Rev. A **30**, 2775 (1984).
[35] H. R. Griem, Phys. Rev. A **28**, 1596 (1983); **38**, 2943 (1988).
[36] L. A. Vainshtein and U. I. Safronova, At. Data Nuc. Data Tables **21**, 49 (1978).
[37] E. J. Iglesias and H. R. Griem, J. Quant. Spectrosc. Radiat. Transfer (to be published).
[38] Hans R. Griem, *Plasma Spectroscopy* (McGraw-Hill, New York, 1964).
[39] D. R. Bates, A. E. Kingston, and R. W. P. McWhirter, Proc. R. Soc. London Ser. A **267**, 297 (1963).
[40] D. R. Bates and A. E. Kingston, Planet. Space Sci. **11**, 1 (1963).
[41] R. W. P. McWhirter and A. G. Hearn, Proc. Phys. Soc. London **82**, 641 (1963).
[42] T. Fujimoto, J. Phys. Soc. Jpn. **47**, 265 (1979).
[43] T. Fujimoto and R. W. P. McWhirter, Phys. Rev. A **42**, 6588 (1990).
[44] B. M. Penetrante and J. N. Bardsley, Phys. Rev. A **43**, 3100 (1991).
[45] Yongzhang Leng, Ph.D. thesis, University of Maryland, 1994 (unpublished).
[46] H. M. Milchberg, I. Lyubomirsky, and C. G. Durfee III, Phys. Rev. Lett. **67**, 2654 (1991).
[47] W. H. Press, S. A. Teukolsky, W. T. Vetterling, and B. P. Flannery, *Numerical Recipes in C: The Art of Scientific Computing* (Cambridge University Press, New York, 1992).
[48] C. Wülker, W. Theobald, F. P. Schäfer, and J. S. Bakos, Phys. Rev. E **50**, 4920 (1994).

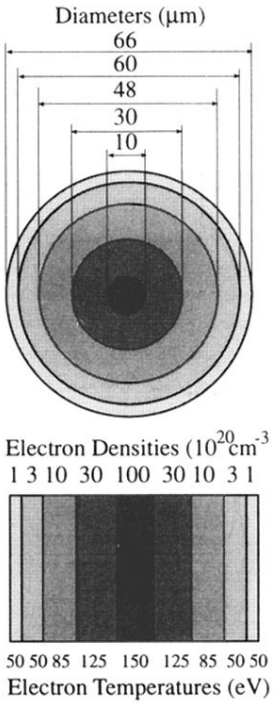

FIG. 3. Geometry of the multilayer model. In computer simulations, the outer layers in the planar model are actually enlarged to have the same volume as the corresponding cylindrical shells.